Responsive spiral photonic structures for visible vapor sensing, pattern transformation and encryption

Jing Qian[1], Srikanth Kolagatla[2], Aleksejus Pacalovas,[2] Xia Zhang[1], Larisa Florea[2*], A. Louise Bradley[1*], Colm Delaney[2*]

[1]School of Physics and AMBER, SFI funded research Centre for Advanced Materials and Bio-Engineering Research, Trinity College Dublin, Dublin 2, Ireland.

E-mail: BRADLEL@tcd.ie

[2]School of Chemistry & AMBER, The SFI Centre for Advanced Materials and BioEngineering Research, Trinity College Dublin, Dublin 2, Ireland.

E-mail: FLOREAL@tcd.ie; CDELANE5@tcd.ie

J. Qian, X. Zhang, A. L. Bradley

School of Physics and AMBER

The SFI Research Centre for Advanced Materials and BioEngineering Research

Trinity College Dublin

Dublin 2, Ireland

E-mail: JQIAN@tcd.ie; ZHANGX4@tcd.ie; BRADLEL@tcd.ie

S. Kolagatla, A. Pacalovas, L. Florea, C. Delaney

School of Chemistry & AMBER

The SFI Centre for Advanced Materials and BioEngineering Research

Trinity College Dublin

Dublin 2, Ireland

E-mail: KOLAGATS@tcd.ie; FLOREAL@tcd.ie; CDELANE5@tcd.ie

Abstract:

Two photon polymerisation using direct laser writing is a burgeoning field of research, with recent focus being placed on bringing added value to microstructures, by incorporating soft, responsive polymers. Moving to the micron-scale can have a profound impact on such stimuli-responsive materials, whose speed of actuation can be increased many-fold compared to their mm-scale counterparts. Here, we report on 4D printing of submicron 2D photonic structures, based on a vapor-responsive photoresist with a refractive index less than 1.55, in the visible wavelength range. The fabricated concentric spiral arrays were evaluated for their feasibility as vapor sensors by testing spectral and structural color reproducibility and reversibility under water, ethanol, isopropanol, and acetone vapors. This approach allows for the realization of predictable uniform color displays which can be modulated upon stimuli response. The transmitted colour in the dry and hydrated states can be accurately modelled. We use this knowledge to design and demonstrate structures for cloaking and image transformation. Such capability can be used for encryption and anti-counterfeit applications.

Keywords: 4D printing; responsive structures; vapor sensing; encryption; structural color

1. Introduction

For more than 500 million years, nature has found ways to generate structural color from natural organisms. The vibrancy and dynamism of these spectacles are attributed to the promotion of pollination, mating displays, and even survival, but the many mechanisms at play to produce this structural coloration are only a relatively recent discovery.[1] With the in-depth exploration of the microscopic world, people marvel at the vibrancy and diversity of bio-photonic structures occurring in nature. Structural color is often more vibrant than pigmentation and is typically directional. Researchers have been inspired for example, by thin film reflectance of *Morpho* butterfly wings,[2] the 3D photonic crystal structure of opals and chameleon skin,[1d, 3] the spongy nanostructures of the feathers of the Kingfisher, *Alcedo atthis*,[4] and the chiral photonic crystal of the *Chrysina gloriosa* beetle.[5] The refractive index (RI) of the main chemical components of these biological exoskeletons is in the range of 1.4-1.8, i.e. chitin (RI~1.56),[2, 6] chitosan (RI~1.52),[7]

guanine (1.5-1.83).[8] While scientists now understand that such structural coloration in the animal kingdom results from complex combinations of multilayer reflectors, diffraction (from periodic surface features with size ~λ), scattering (by non-periodic structures with size > λ), and photonic crystals and higher-order photonic materials, synthetic analogues have remained difficult to reproduce. Recent work has made notable steps in recreating structural coloration seen in nature, using multilayers,[9] or replicating assembled colloidal patterns in inorganic materials.[10] These approaches result in 2D surface gratings but fall short in replicating the complexity and dynamic effects of natural systems. To truly achieve integrated responsive optical elements combining 3D photonic band gap materials with adaptable structural hierarchies (in 2D and 3D), it is imperative to 1) move away from classic etching, anodizing, and deposition techniques and 2) develop suitable materials beyond inert high refractive-index dielectrics.

Fabricating dynamic photonic devices inspired by nature, would not only serve to create high-resolution printing with high color-brilliance and non-fading properties,[11] but offers a pathway to active display technologies,[12] biometric recognition,[13] steganography,[11b, 11c, 14] and polarisation encryption.[15] Difficulties in achieving 3D fabrication of stimuli-responsive photonic materials, from the macroscale to nanoscale, has remained one of the barriers to realizing such structures. This is mainly due to the soft nature of the hydrogels, their tendency to collapse (e.g. woodpile hydrogel structures[16]) and the sparsity of 3D fabrication technologies that are both compatible with hydrogel materials and can also achieve sub-micron resolution, as a key requirement for the realization of photonic structures.

In the past five years, direct laser writing (DLW) by multi-photon polymerization has been successfully used in the fabrication of complex photonic structures yielding vibrant and tunable structural colors over a wide gamut of the visible spectrum.[11, 17] While these studies have shown that such photoresists can be fabricated into multi-dimensional photonic crystals with rich structural colors, generally they are non-responsive,[10e, 17b-g] and the resulting structural colors static in nature. In this regard, the development of smart hydrogels has brought great potential to photonic crystals, through their reversible response to external stimuli such as pH, temperature, humidity, light, and magnetic field.[18] This provides a direct route to the exploitation of 4D printing for the creation of wide-gamut dynamic structural color.

Herein, we present 2D photonic spiral arrays comprising an acrylamide-based hydrogel. We exploit Finite-Difference Time-Domain (FDTD) simulation to predict the colors and optical response of different designs in vapor and liquid states, which are supported by experimental results. We note that the observed hue is not significantly affected by the spacing of lines, as for other line-based 2D photonic structures in the literature,[11a, 17a] but rather by line width (d) and height (h). Variation of height provides a wider color gamut than variation of linewidth for the same micro color pixel size. This vapor-responsive hydrogel exhibits reversible expansion and contraction states when exposed to varying vapor or liquid environments (water, ethanol, isopropanol, acetone), which constitutes the fourth dimension. Using simulation we can predict and fabricate a wide gamut of structural colours, that we further combine with the inherent stimuli-response of the material, to modulate the color displays.

We further expanded the vapor study to liquid environments to demonstrate structural colour of the hydrogel structure arrays in the liquid state. This represents, to our knowledge, the first instance in which structural coloration is obtained for hydrogel materials ($RI_{dry\ polymer} < 1.5$) in the submerged state. Arrays comprised of pixels of different heights were also used to reveal or conceal patterns upon changes in the surrounding medium. This work provides a blueprint for the application of 4D printing based vapor and liquid sensing, and chemo-responsive anti-counterfeiting displays.

2. Results and Discussion

We have previously presented direct laser writing of an acrylamide-based photoresist which displayed structural coloration when fabricated into periodic grid arrays.[17a] By directing this fabrication with comprehensive FDTD simulations, we have now developed a family of concentric square spirals of varying size and periodicity which display enhanced response in the vapor state and structural color in different solutions. Compared to the grid structure, the new concentric spiral structures allow for an improve ratio of polymer to void within the unit cell, thereby improving the color intensity of the visible structural coloration not only in air and vapor environments (n~1) but also in much higher refractive index environments (i.e. water). Furthermore, as each concentric frame is isolated from the array, its expansion is less restricted compared to a continuous connected grid-like structure, while the increased surface area of the

structures ensures improved interaction with the surrounding media. A schematic of such an array and the relevant dimensions of the individual concentric square spirals are shown in Figure 1a. The structure is defined by three gaps in addition to varied height and linewidth. The structures were fabricated using a commercial Nanoscribe GT Professional system, as depicted in Figure 1b, to obtain 300 µm × 300 µm arrays of concentric square spirals (Figure 1c). The arrays were optically characterized using a custom-built transmission spectroscopy apparatus, shown in Figure S1a (Supporting Information), with further details provided in the Experimental section. Numerical simulations were performed using Lumerical FDTD commercial software. A schematic of the simulation is shown in Figure S1b (Supporting Information), and the details are provided in the Experimental section. The refractive index as a function of wavelength for the hydrogel was measured using spectroscopic ellipsometry and the results are shown in Figure S2a-b (Supporting Information). The simulated transmittance spectra of one such family of structures based on an 11-line (11L) array (g1 = 2 µm, g2 = 1.5 µm, g3 = 1.5 µm, s = 9.5 µm), are shown in Figure 1d-e. For a constant d = 0.9 µm, with increasing structure height, a significant red shift in transmittance maxima can be observed in Figure 1d. Similarly, with constant h = 2.0 µm and s = 9.5 µm, a less dramatic red shift is observed with increasing structure linewidth, shown in Figure 1e. The structural colors of the arrays corresponding to the spectra in Figures 1d and 1e are plotted in the CIE 1931 chromaticity diagram in Figure 1f. It can be observed that varying the structure height (blue points) results in a wider gamut of color than varying linewidth (red points). Furthermore, it must be noted that an increase in refractive index of the medium, or a decrease in refractive index of the material, are both predicted to induce blue shifts of the transmittance maxima (Figure S3a, Supporting Information). These parameters, which drive the red and blue shifts of the transmittance spectra, are important for the subsequent analysis of structural color changes in vapor sensing and information encryption.

The spiral structure presented herein acts as a 2D transmission phase grating,[19] and shows strongly angle-dependent diffraction properties, as shown in Figure S2c and S2d. The zero-order transmittance spectra are determined by the interference between the light which passes through the hydrogel lines and the light which passes through the gaps. Constructive interference requires a phase difference $\Delta\phi = k_0(n_{hydrogel}-n_{gap})h = 2\pi m$, where m is an integer, n is the refractive index, $k_0 = 2\pi/\lambda_0$ and λ_0 is the wavelength in air. Therefore, the peak wavelengths in the transmittance

spectra are given by $\lambda_0 = (n_{hydrogel}-n_{air})h/m$, and the calculated peak wavelengths are seen to be in close agreement with the simulated spectra m=1 to 3, shown in Figure S3c(i). Similarly, a blue shift of the transmission peaks is expected as the gap is filled with a higher refractive index media, such as water, as illustrated in Supporting Information Figure S3b. In this case the peak wavelengths are calculated using $\lambda_0=\{n_{hydrogel}.h-[(n_{liq}.t_{liq})+ (n_{air}.t_{air})]\}/m$ where t_{air} represents the height of the volume gap filled with air, t_{liq} represents the height of the liquid in the gap, and $t_{liq} + t_{air} = h$. The calculated blue shifted peak position (dashed lines) are also in agreement with the simulated peaks shown in Figure S3c(ii). This simplified description provides insight into the underlying physics of the transmission phase grating and describes the dominant spectral characteristics. However, this does not capture the full complexity such as the spectral dependence of the transmission peak on the linewidth seen in Figure 2e.[19c] Consequently, the FDTD numerical simulations are used for the structure design.

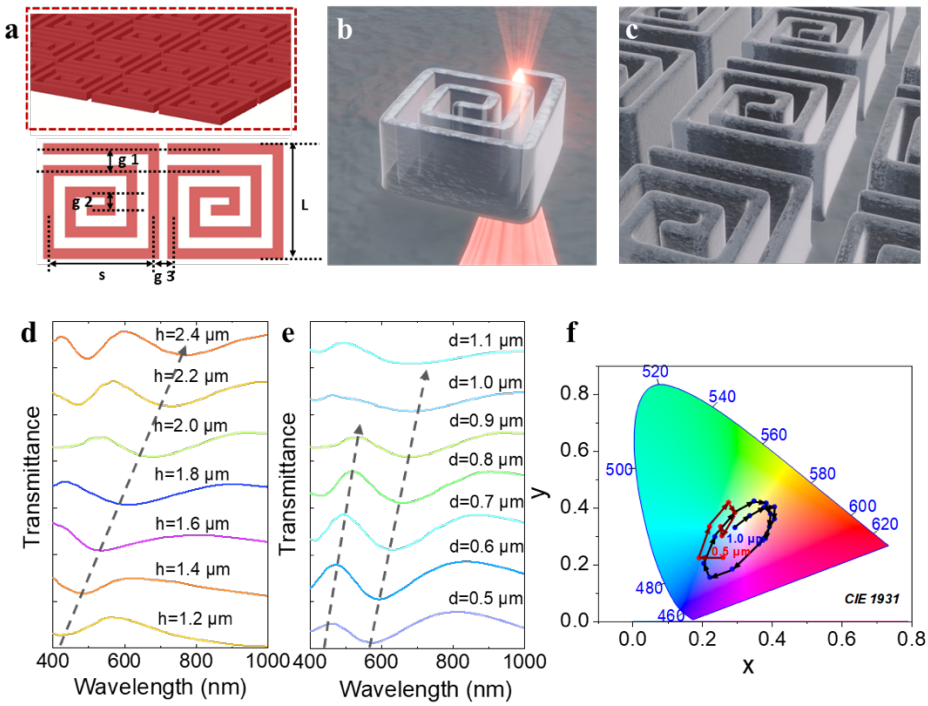

Figure 1. Fabrication and design of a 300 μm × 300 μm 11L spiral photonic array. a) Schematic of 11L photonic array design. The design dimensions of 11L spiral are: g1 = 2.0 μm, g2 = g3 = 1.5 μm, s = 9.5 μm, d =0.5 μm, and L = 10 μm. b) Schematic shows an example of the fabrication of a single 11L spiral structure by two-photon lithography (TPL). c) representation of the spiral photonic array. d) FDTD simulated transmittance spectra of 11LF array with d = 0.9 μm, s=9.5 μm, g1 = 2.0 μm, g2 = g3 = 1.5 μm and h ranging from 1.2 μm to 2.4 μm with an interval of 0.2 μm. e) FDTD simulated transmittance spectra of 11L spiral array with h=2.0 μm, s=9.5 μm, g1 = 2.0 μm, g2 = g3 = 1.5 μm and d ranging from 0.5 μm to 1.1 μm with interval of 0.1 μm. f) CIE 1931 chromaticity diagram shows the simulated color coordinates of the structure designs in (d) and (e).

Three hydrogel photonic sensors (HPS) based on 11L spiral arrays were printed using design parameters g1 = 2 µm, g2 = 1.5 µm, g3 = 1.5 µm, s = 9.5 µm and d = 0.5 µm (as in Figure 1a), a slicing distance of 300 nm, hatching distance of 200 nm, two contour lines (contour distance 100 nm) and at laser powers of 25 mW (HPS 1), 27.5 mW (HPS 2) and 30 mW (HPS 3). Figure 2a-c show examples of HPS 2 characterized by scanning electron microscopy (SEM) and atomic force microscopy (AFM). The SEM image, shown in Figure 2a, of a single 11L spiral structure of HPS 2 demonstrates the structural integrity and stability of the TPL-printed 11L spiral. The structural homogeneity of HPS 2 array is demonstrated by the AFM image in Figure 2b. A 3D profile of HPS 2 array is shown in Figure 2c. To truly understand the homogeneity in height using AFM, a greater spacing between adjoining features was necessary. This is shown for an extended spiral structure in Figure 2d, with identical design and printing parameters, but increased distance between lines. Figure 2e shows the height analysis along trace shown in Figure 2d and exhibits the structure uniformity and homogeneity. Critically, the resulting structures are shown to retain their hydrogel properties. Using AFM force curve measurements, the average Young's modulus in air is 244±4 MPa, and upon hydration this is decreased to 20.2±0.8 MPa. Retention of its soft properties and ability to significantly swell, is critical for the development of responsive structures *via* TPL. Other commercial photoresists, such as IP-Dip and IP-L, display Young's modulus values of 2.1 GPa and 4.3 GPa, and show minimal uptake of water.[20]

The experimental zero-order transmittance spectra of HPS 1, HPS 2 and HPS 3 are shown in Figure 2f. FDTD simulations informed by measured dimensions of the fabricated structures yielded the spectra shown in Figure 2g (HPS 2) and Figure S4c (Supporting Information) for HPS 1 and HPS 3. The heights used in the simulations are listed in Figure S4e (Supporting information), which are within the range obtained from the SEM and AFM measurements in Figure S4 (Supporting information). This confirms that the hydrogel structures can be fabricated with high accuracy and good fidelity to the design parameters. At constant writing speed (10,000 µm/s), it is worthy of note that varying power in small increments from 25-30 mW, has a small impact on both height and width of features (approximately a 50 nm increase in feature height and width per 2.5 mW increase in laser power). These are documented in greater detail in Figure S4 (Supporting Information).

TPL hydrogel structures show great promise for sensing applications. In this regard, we probed the response of the square spiral to a range of solvent vapors, to understand the swelling of the hydrophilic structures and to assess their potential. In the first instance we examined the transmittance spectra of HPS 2 in response to water vapor (flowrate 0.3 L/min for 5 min), shown in Figure 2h. The red shift of FDTD spectrum for HPS 2 can be clearly seen. The observed change in the transmittance spectrum of HPS 2 exposed to a flow rate 0.3 L/min can be simulated by considering structure expansion in height and linewidth by 3.5%. It should be noted that the redshift in the transmittance spectrum due to the increase in height and linewidth competes with the spectral blueshift caused by the increase in the refractive index of the voids. The maximum expansion of fully hydrated 11L spiral structures was measured by AFM to be 9 ± 1% across 3 different laser powers (25-30 mW). The AFM analysis is shown in Figure S5.

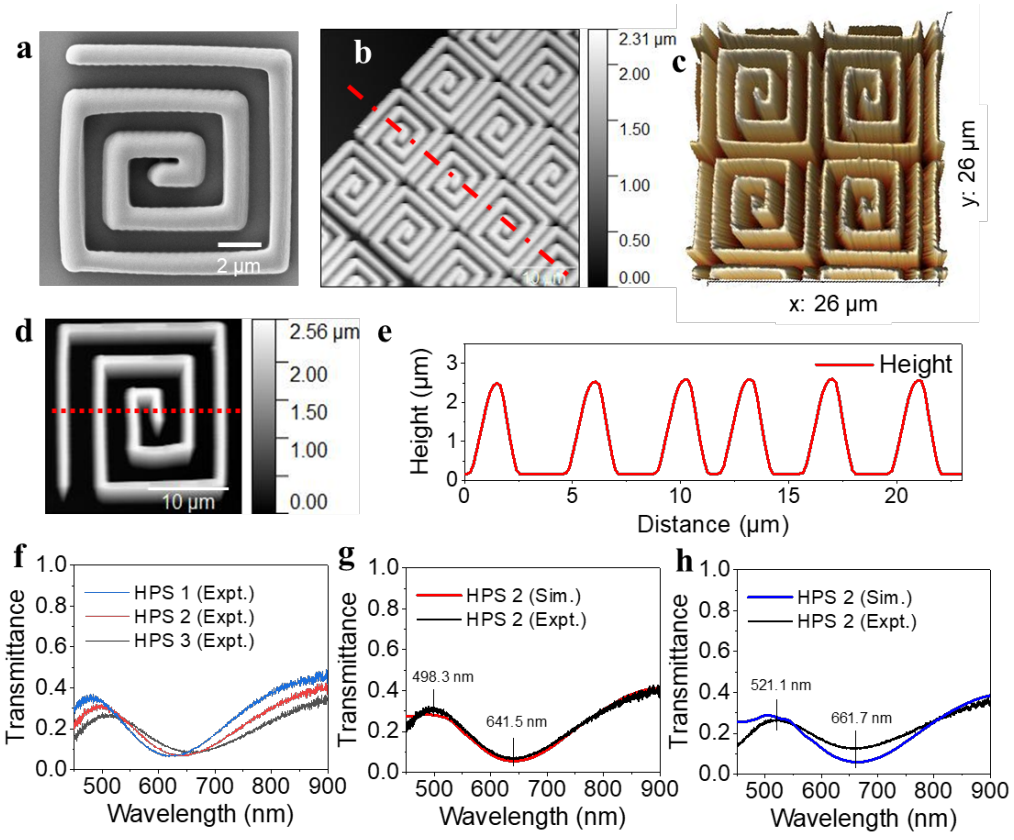

Figure 2. Characterization and optical properties of 11L concentric square spiral photonic arrays. a) Top-down SEM image of a representative 11L HPS 2 concentric square spiral. b) Atomic force microscopy (AFM) demonstrates the homogeneity of HPS 2. The height analysis across the red trace is shown in Figure S4d. c) AFM image shows the 3D reconstruction of HPS 2 structure in tapping mode. d) AFM image of an extended 11L concentric square spiral printed by 27.5 mW laser power (HPS 2) and height analysis across the red trace is shown in e). f) Zero-order transmittance spectra of HPS 1, HPS 2 and HPS 3. Comparisons of simulated and experimental zero-order transmittance spectra of HPS 2 in g) air and h) water vapor environment (0.3 L/min flowrate for 5 minutes).

To investigate the possibility of employing this acrylamide-based photoresist to fabricate hydrogel structures capable of optically responding to a range of solvent vapors, we explored the effect of exposing the arrays to four solvent vapors (water, ethanol, isopropanol and acetone). A gradual red shift in peak wavelengths and a clear modulation of transmittance at both maxima is observed with increasing solvent polarity (acetone < isopropanol < ethanol < water), shown in Figure 3a(i). Figure 3a(ii) shows ΔT/T as a function of wavelength for the four vapor exposures at a flowrate of 0.3 L/min for 5 minutes, where ΔT is the change in transmittance ($\Delta T = T_{vapor} - T$), T is the dry state transmittance, and T_{vapor} is the transmittance for the exposed structure. The dependence of this response on flowrate (for water vapor) can be seen in Figure 3b. The increased flow rate corresponds to increased humidity as measured using a commercial humidity sensor (TSP01 Thorlabs), shown in Figure S7d (Supporting information). The flowrate range of 0.05 L/min to 0.3 L/min corresponds to a humidity range of ~56% to 90%. It is evident that the wavelength and ΔT/T values increase with increased vapor concentrations.

Figure 3c shows the variation in transmittance of HPS 2 at 498.8 nm (peak, dotted line) and 641.9 nm (trough, solid line) over time, upon exposure cycles to the various solvent vapors. The time sequence is depicted in more detail in Figure S6a (Supporting information). In addition to fast response times and reproducibility of the response, a clear trend in response to solvent polarity (acetone < isopropanol < ethanol < water) and concentration can be observed. Secondly, the absolute ΔT values are larger at higher flowrates for water vapor, ethanol vapor and isopropanol vapor, but not in the case of the acetone vapor. Acetone shows a different behavior to the other three solvents. At the lowest flowrates ΔT for acetone vapor is higher than for isopropanol, and the response time is faster. However, the response to acetone quickly saturates, and for flowrates above 0.15 L/min no further change in ΔT is observed. The spectral shift (Δλ) of the peak-and trough versus time are plotted in Figures 3d and Figure S7c (Supporting Information). Overall, the trends for Δλ are similar to those observed for ΔT, but it can be noted that measurement of ΔT offers greater differentiation in the response of the structure to the different solvents. It was also confirmed that while the spiral structures fabricated at laser powers between 25 mW and 30 mW show the same trends, the structures fabricated with the higher laser power show larger change in their transmittance spectra, shown in Figure S6b-c and S7a-b (Supporting information). This is attributed to an increased volume of hydrogel.

To further analyse the flowrate dependence for each vapor, Figure 3e shows ΔT/T at 641.9 nm as a function of flowrate, with a vapor exposure time of 5 minutes. The numbers associated with each line correspond to the slopes of the fitted curves. We observe that, except for the least polar solvent (acetone), the ΔT/T values for water vapor, ethanol vapor, and isopropanol vapor exhibit two distinct ranges with linear dependences. At lower flow rates ΔT/T is more strongly influenced by changes in flow rate, while at the higher flow rates ΔT/T is less sensitive to further increases in flowrate. The slopes of the fitted curves for flowrates of 0.2 L/min to 0.3 L/min decrease compared with that in the 0.05 L/min to 0.2 L/min range because the higher flowrates accelerate the evaporation of the solvents and reduce the interaction with the polymer structures. The change in peak wavelength of 11L HPS 2 as a function of the flowrate is presented in the Figure S7.

To further comment on sensitivity of the 11L HPS 2, the rise time is extracted. The function $\Delta T=\Delta T_0+A(1-\exp(-t/\tau))$ was used to fit ΔT in Figure 3c for each vapor at 641.9 nm (trough) across different flowrates, where ΔT and t are the y and x axis values in Figure 3c, ΔT_0 (offset of ΔT from 0 point), A (an amplitude factor) and τ (characteristic response time) are fitting variables. Characteristic response time results are shown in Figure 3f. As expected, the response time is inversely proportional to the vapor concentration (flowrate). The response times of HPS 2 to water vapor, ethanol vapor and isopropanol vapor are all less than 200 s in the range of flowrate 0.15-0.3 L/min under our current experimental conditions using a rudimentary bubbler system, with isopropanol and acetone showing the longest and shortest response times, respectively. The observed experimental trend in response time is a combination of two opposing effects: the vapor pressure of the solvent (acetone > ethanol > isopropanol > water) and the solvent polarity (water > ethanol > isopropanol > acetone) where solvents of higher vapor pressure are easier to evaporate using the same flow rate, while solvents of higher polarity will cause a higher degree of swelling of the hydrogel network. The different response time for different vapors for hydrogel photonic sensors demonstrates their potential for mixed vapor measurements.[21]

The principle of this hydrogel photonic sensor is to detect various vapors based on structure color change in the transmission, combined with FDTD simulations and AFM results, which are mainly due to the structure expansion. The color change of the structure of this HPS under the expansion mechanism can also be maximized by optimizing the periodic structure. There have been some reports using the same structural color change mechanism to design vapor sensors, for example,

1D photonic crystals (i.e. optical fibre, Bragg reflector),[22] hybrid 2D photonic crystal slabs,[23] colloidal nanoparticles embedded in responsive hydrogels.[24] In addition, some multi-dimensional photonic crystal designs based on non-responsive hard resins,[21a] inorganic or metal oxides,[22b, 25] whose structural color change mechanism is the change of medium refractive index, where some of these designs have been shown to have great potential in multivarious vapor sensing.[21a, 22b] Liquid crystal materials are another class of materials often used to design vapor sensors by detecting color change. They have unique material properties and are typically designed to change the pitch of helix by swelling or contracting to enable vapor detection.[25] Compared with the studies reported above, this micron-scale hydrogel photonic sensor has great flexibility in terms of structural design and dimension. This means that in a short time, low energy consumption and low-cost conditions, it is possible to fabricate any shape sensor to adapt to the application environment and equipment requirements.

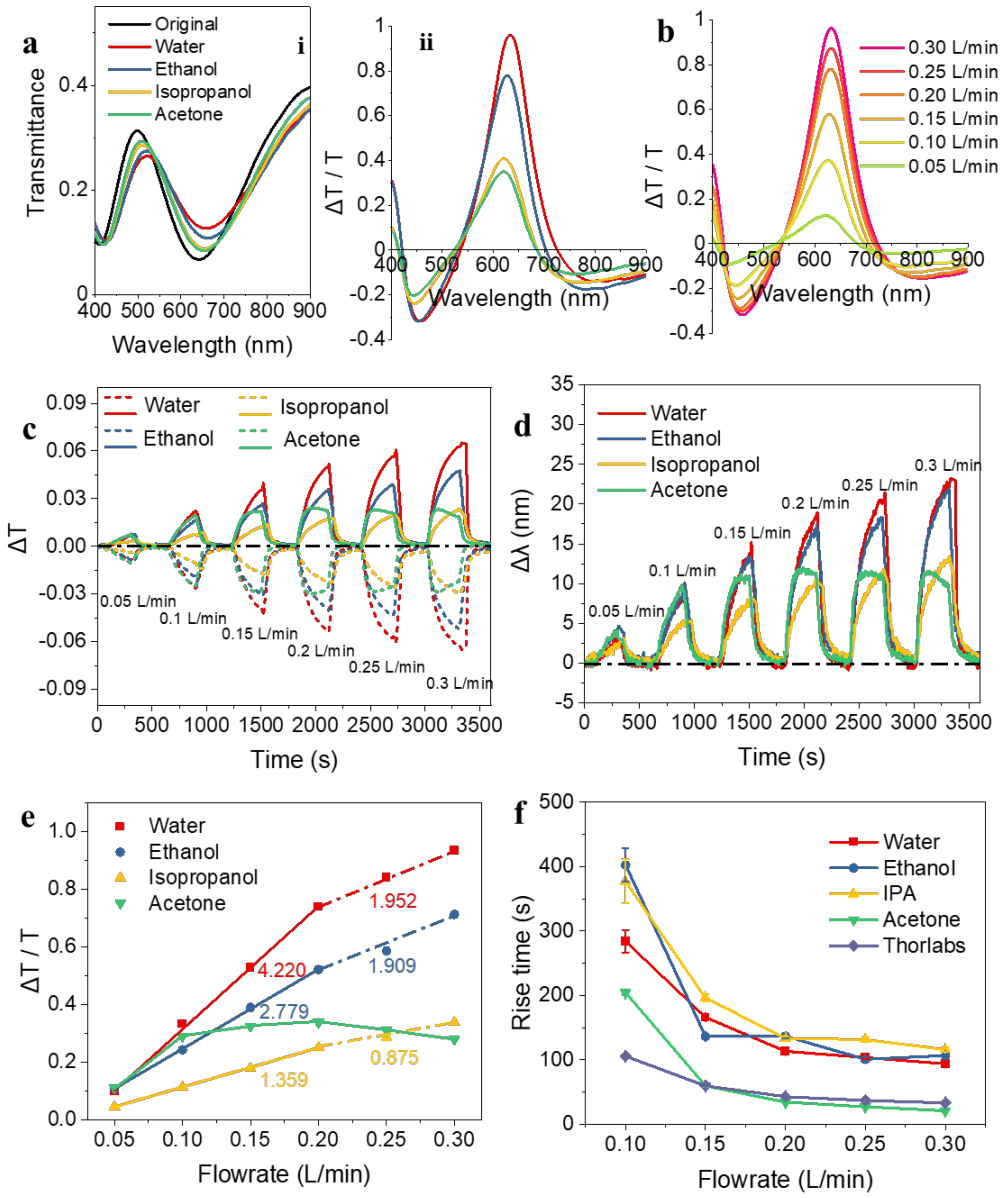

Figure 3. Vapor sensing tests of 11L concentric square spirals array. a) i) Transmittance of 11L HPS 2 in air and under water vapor, ethanol vapor, isopropanol vapor and acetone vapor (flowrate 0.3 L/min for 5 min). ii) The corresponding ΔT/T versus wavelength. b) ΔT/T versus wavelength for a range of flowrates from 0.05 L/min to 0.3 L/min. c) Change in transmittance (ΔT) of 11L HPS 2, as a function of exposure time at the 498.8 nm peak (dotted line) and 641.9 nm trough (solid line). d) Change in peak wavelength of 11L HPS 2 as a function of exposure time. e) Δ T/T versus flowrate at 641.9 nm, inserted values represent slope of fitted line. f) Rise time versus flowrate analyzed from c) and Figure S7d.

A square spiral structure composed of 5 lines (5L) was designed as shown in Figure 4a, with shorter line length (L = 5.5 µm) and smaller area size, to minimize structural deformations upon complete hydration. FDTD simulations were firstly used to investigate the influence of structure linewidth (d), height (h), refractive index (RI) upon immersion in solvent on the zero-order

transmittance spectra. Results are shown in Figure S8 (Supporting Information). As previously seen changing the height of the structure offers a means to design color pixels, with a wide color gamut. The colors corresponding to simulated transmittance spectra for structures of varying height in Figure S8a are shown in Figure S8f (blue dots).

Eleven 5×5 5L spiral arrays (47.5 μm × 47.5.5 μm in x and y directions) with design height variation from 1.0 μm to 3.0 μm were fabricated by TPL and their zero-order transmittance color in air, captured by a 4X objective lens (NA=0.1), is shown in Figure 4b. 45˚, 75˚ and 90˚ tilted SEM structural characterization in Figure S9a (Supporting information) show the printed 5L spiral arrays with a design height of 2.0 μm. These 5L spirals were fabricated with an underlying film (0.6 μm) to increase uniformity. Figure S9b-d (Supporting information) show AFM height analysis for pixels with structure height of 1.0 μm (above film). Height analysis of all 5L spiral structures are listed in Table S1 (Supporting information). The reproducibility of the printed color pixels was also confirmed, as seen in Figure S9e (Supporting information). The zero-order transmittance spectra of the arrays are shown in Figure 4d, and the corresponding structure colors are plotted in CIE 1931 chromaticity diagram (red dots) in Figure S8f (Supporting Information). The FDTD simulated transmittance spectra in Figure 4e show good agreement with experimental results in Figure 4d. The detailed fitting dimensions are listed in Table S1 (Supporting information). The structural colors of the pixels in IPA are shown in Figure 4c. The 5L spiral arrays exhibit a large blue shift of the peak wavelength $\lambda_0 = (n_{hydrogel}-n_{IPA})h/m$, as the refractive index difference between the gaps and the hydrogel is reduced when immersed in IPA, $n_{IPA} = 1.377$.[26] Further simulations showing the effect of IPA is shown in Figure S8d and corresponding AFM height analysis for pixels in air and in IPA is provided in Table S1 (seen Supporting Information). The zero-order transmittance spectra in IPA in Figure 4f match well with FDTD simulations in Figure 4g. The fit is achieved using an 8% linewidth and height expansion as well as the presence of the IPA in the gaps. The refractive index is calculated through Maxwell-Garnett effective medium theory.[27] 8% is the average (n=6) expansion of 5L spiral arrays in IPA, which is calculated through AFM height analysis of samples (details see Figure S9 and Table S1 in supporting information). In this case for completeness, we included the change in refractive index of the hydrogel when immersed in IPA, but it should be noted that it has a negligible effect as the reduced refractive index contrast between the structure and surrounding medium results in the dominant blue-shift of the spectra.

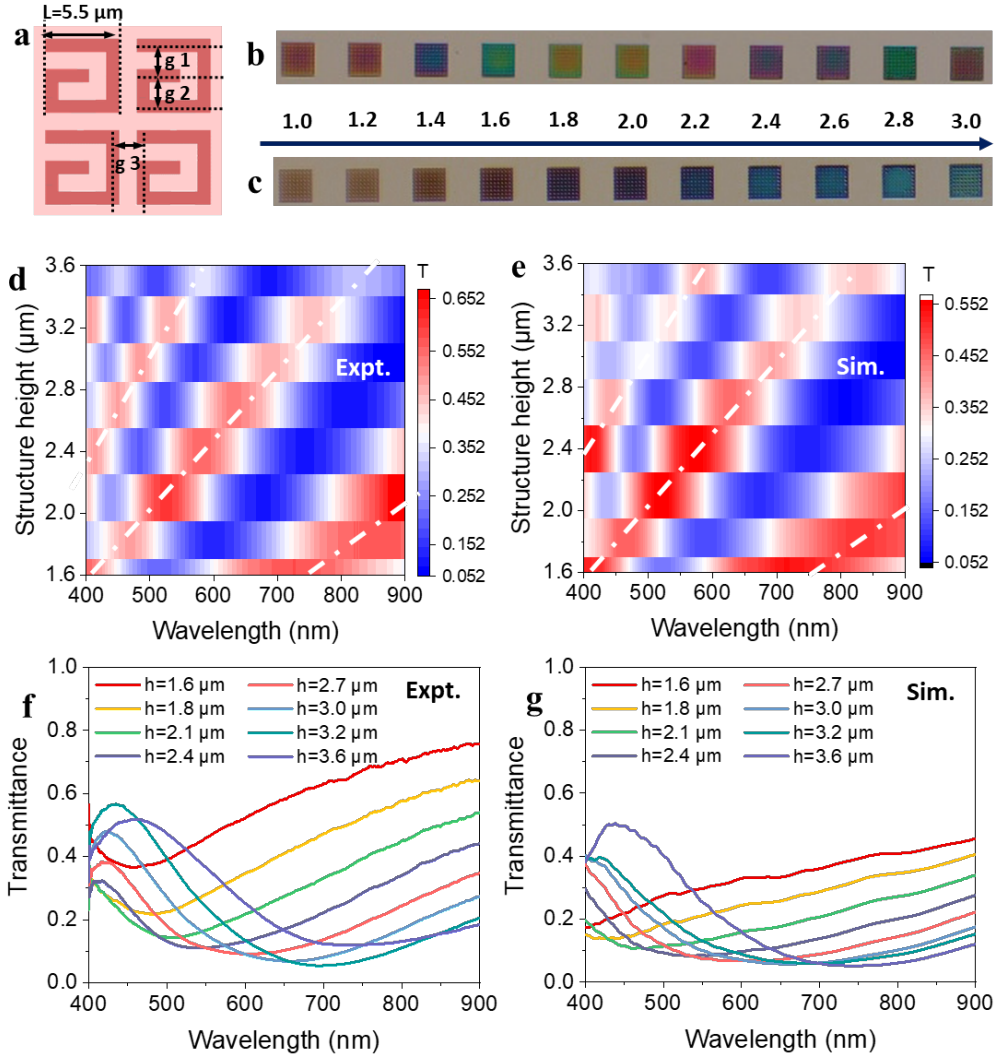

Figure 4. 5L square spiral color pixels. a) Schematic of 5L spiral photonic structure design with a 0.6 µm thick film underneath (d=0.5 µm, g1 = g2 = g3 = 2.5 µm). b) and c) The color pixels in air and IPA solvent, respectively, composed of 5 × 5 5Ls (37.5 µm × 37.5 µm) with design heights ranging from 1.0 µm to 3.0 µm. Contour plots show d) experimental zero-order transmittance versus wavelength and e) FDTD simulated transmittance versus wavelength and simulation heights. The simulation heights and linewidths are given in Table S1. The white dashed lines serve as a guide to the eye. f) and g) Experimental and simulated zero-order transmittance spectra in for the structures immersed in IPA liquid with n_{IPA} = 1.377, respectively. An increase of 8% in linewidth and height is considered in (g).

TPL brings flexibility to the fabrication of complex microscale patterns, enabling fine-tuning of observed color and response. Some humidity-responsive patterns were designed using the 5L square spiral array, and visible color changes can be seen in Figure S10 (Supporting Information). Further inspired by the color change of the 5L spiral array in IPA (Figure 4b), we explored the inclusion of image encryption. Some novel designs are shown in Figure 5, and we have demonstrated incredible potential for image and information encryption, concealment, and

transformation. All examples have a linewidth design of 0.5 µm. Figure 5b(i) and (iv) show an example of a heart pattern being revealed upon immersion in solvent. The heart pattern pixels are designed with h=2.8 µm while the background pixels have height of 1.6 µm, as depicted in Figure 5a. Figure 5(ii) and 5(v) show an example of color transformation for both the background and the heart pattern. In this case the background and heart regions had h=1.6 µm and 2.6 µm, respectively. An example of information transformation is shown in Figure 5b (iii) and (vi), with the purple heart pattern transforming into to a square pattern upon immersion in IPA. This heart pattern is designed with inner square with 5L spiral of h=1.4 µm, the outer heart region with h=2.6 µm and background with h=2.8 µm. SEM images in Figures 5c and 5d show the heart pattern and inner square designs corresponding to Figures 5b(i) and (iii). The zero-order transmittance spectra in Figure 5e show that the dominant peak in the visible spectrum occur in the same spectral range for the heart and background regions in Figure 5b(i). The structural response can also encode and encrypt information, for example a QR (quick response) code (Video S1). The examples in Figure 5f and 5g show two QR codes activated in solvent, which can be employed in anti-counterfeiting and information security.

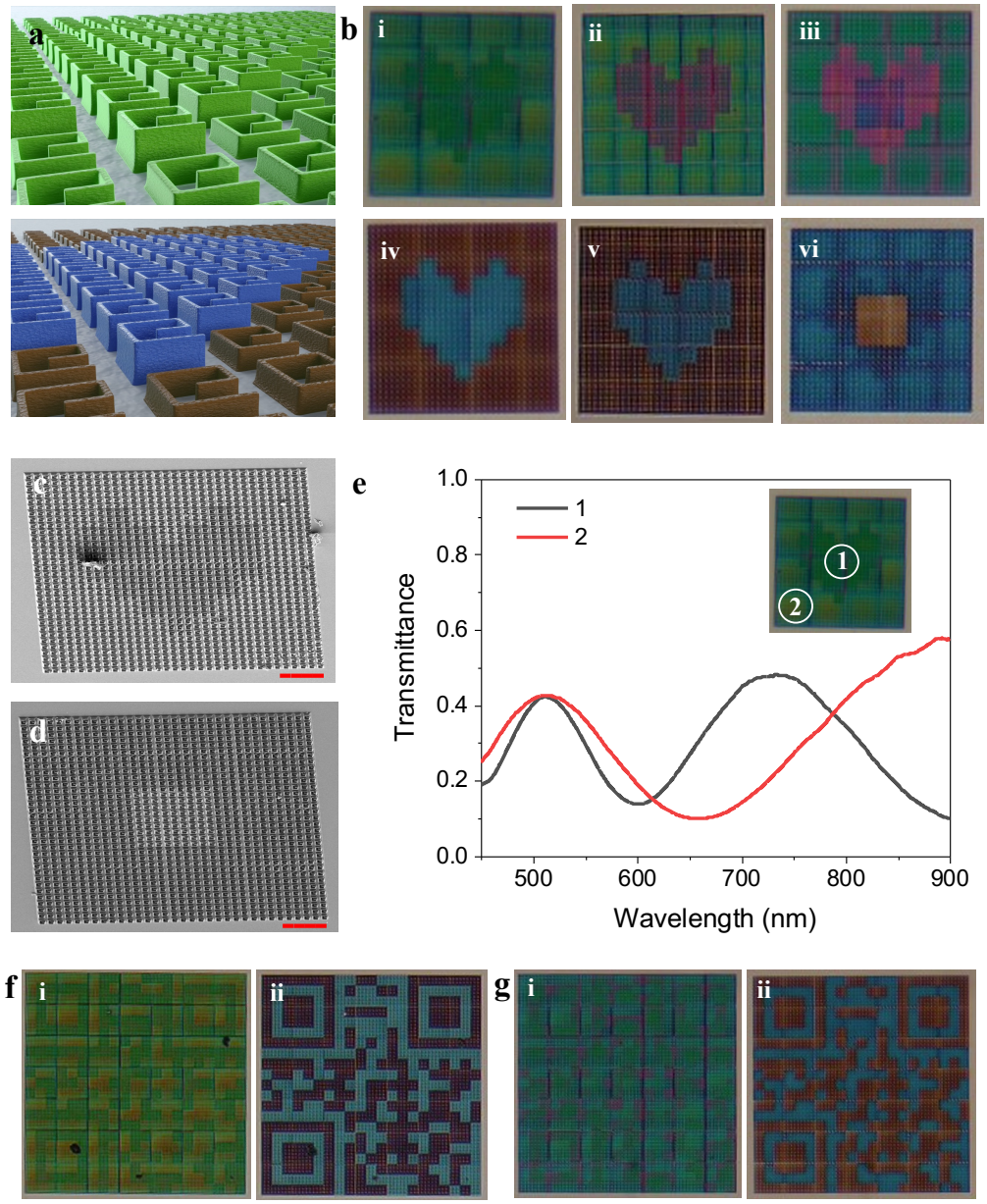

Figure 5. Encryption pattern design. a) Schematic of a heart design comprising 5L spirals, in air (top) and after submersion in IPA (bottom). b) CCD images of i) pattern1, ii) pattern2 and iii) pattern3 in air (top) and after submersion in IPA (bottom) iv), v) and vi) respectively, showing the remarkable color changes that can be achieved. c-d) SEM images of pattern1 and pattern3, respectively. Red scale bar corresponds to 40 µm. e) Zero-order transmittance spectra of areas 1 and 2(see inset) of pattern 1. f-g) Two examples of encrypted patterns in air (left: f(i) and g(i)) and the revealed QR codes decrypted by immersion in IPA (right: f(ii) and g(ii)).

3. Conclusion

We have successfully combined an acrylamide-based vapor-responsive photoresist with two-photon lithography to fabricate submicron 2D multiline photonic structures. The structures were designed using FDTD simulations. The potential to employ the 2D photonic array in a structural

color-based vapor sensor is verified through consecutive vapor response testing and transmittance spectra analysis. The highly repeatable and reproducible results demonstrate the enormous potential of this approach for visible structural color-based vapor sensors. It is clearly demonstrated, using experimental and simulation results, that the increase of structure height and linewidth are the dominant factors producing a spectra redshift and structural color change under vapor exposure. For the maximum vapor flowrate investigated of 0.3 L/min, approximately a 3.5% increase in the height and linewidth of the polymer structure was induced. AFM analysis determined that the swelling limit of such polymer microstructures is approximately (9 ± 1)% when fully submerged in deionized water. The Young's modulus variation under water saturation is decreased over 100-fold, which provides further opportunities to broaden its applications. Furthermore, some novel examples of pattern concealment and transformation were demonstrated using 5L square spiral pixels with possibilities for applications of information encryption, anti-counterfeiting, decoration etc. In this case, the change in structural color is dominated by dramatically blue-shifted spectral features caused by the increase in the refractive index of the ambient medium. In addition to vapor sensing and information encryption mentioned above, the structural coloration obtained in the fully-immersed state indicates a promising approach for the design of hydrogel-based chemical and bio-chemical photonic sensors.

4. Experimental section

Materials and Monomeric Cocktail Preparation: An acrylamide-based photoresist was synthesized as previously reported.[17a] Tetrabutyl phosphonium chloride ([$P_{4,4,4,4}$][Cl]), 80% in water was obtained from TCI, Japan. Acrylamide (Am) 98% as the hydrophilic monomer, trimethylolpropane ethoxylate triacrylate (Mw~912) (TMPET) as the crosslinker, and 3-(trimethoxysilyl) propyl methacrylate 98% were purchased from Sigma Aldrich, Ireland and used as received. 7-Diethylamino-3-thenoylcoumarin (DEATC) photo-initiator was obtained from Alpha Chemical, USA. Anhydrous solvents, i.e. ethanol, 2-propanol (IPA), propylene glycol methyl ether acetate (PGMEA) were obtained from Sigma Aldrich. 2.81 mmol (14.4 wt%) of Am, 0.66 mmol (43 wt%) of TMPET, 0.012 mmol (0.3 wt%) of DEATC and 1.62 mmol (42.3 wt%) of [$P_{4,4,4,4}$][Cl] were mixed to obtain the monomeric cocktail.

Printing of Square Spiral Structures: A commercial direct laser writing system (Photonic Professional, Nanoscribe Gmbh) was used to fabricate the 2D square spiral structures. Structures were all fabricated on high precision coverslips (170 ± 5) µm using a 780 nm femtosecond laser focused though a 63X objective (Zeiss, Plan Apochromat) in oil immersion configuration. Lens oil (Zeiss Immersol 518F) was purchased from Zeiss. Prior to fabrication, the high precision coverslips (Thermo Fisher Scientific) with accurate thickness of (170 ± 5) µm were cleaned by sonication in ethanol (30 minutes) followed by activation using 15 minutes UV-ozone treatment (digital UV-ozone system, PSD Pro Series) and silanisation using 3-(trimethoxysilyl) propyl methacrylate (Sigma Aldrich) to ensure covalent attachment of the fabricated microstructure to the glass substrate.[28] The schematic diagram of the printing configuration is shown in Figure 1b. An objective lens is immersed in oil and a drop of the hydrogel cocktail was placed on top of the substrate. The structure stl. file was imported into DeScribe 2.4.4 software, with 0.3 µm slicing distance and 0.2 µm hatching distance and 0.1 µm contour distance. 25 mW, 27.5 mW and 30 mW laser power and 10K µm/s writing speed were applied to fabricate the HPS 1, HPS 2, HPS 3 (11L spiral) array. For the 5L color pixel printing, the laser power and writing speed were fixed at 25 mW and 10K µm/s, respectively. The structures were then rinsed with isopropanol, followed by drying under nitrogen after fabrication.

Numerical Simulations: Lumerical software, finite difference time domain (FDTD) solution was used to design the structure and fit transmittance spectra. A single spiral structure was defined on a glass substrate. A mesh cuboid was defined to completely cover the spiral structure with 0.1 × 0.1 µm resolution along the x and y axes and 0.01 µm resolution along the z axis. The simulation region model is shown in Figure S1b, with FDTD size of 11 µm in x and y axes for 11L spiral structure and 7.5 µm in x and y axes for 5L spiral pixels. To simulate the single spiral perfectly matched layers boundary conditions were applied in x, y and z directions. The transmission DFT monitors were placed 45 µm and 30 µm above substrates for 11L spiral and 5L spiral, respectively. The wavelength range in simulations were set between 400 nm to 1000 nm. To fit the transmittance spectra the linewidth measured from the SEM images is taken as the reference value. The refractive index of the hydrogel was measured by Ellipsometry system (SOPRA GESP 5 Variable Angle Spectroscopic Ellipsometer). The thin film thickness and refractive index are shown in Figure S2. The refractive indices of the substrate and IPA are 1.5 and 1.377,[26] respectively.

Optical Measurements: A home-built angle resolved setup combined with a simple bubbling system as shown in Figure S1a, was used to capture zero-order transmittance spectra for both 11L and 5L photonic arrays. A collimated white light source (HL-2000-HP from Ocean Insight) was used to illuminate the sample, the transmitted signal was firstly captured by a 5X objective lens (NA=0.12, from PRIOR company), see Figure S1a. The light was then focused into a 20X objective lens (NA=0.4, Olympus Plan Achromat Objective) by a lens with a focal length of 25.4 mm. The transmittance spectra were measured using a fiber-coupled spectrometer (CCS100 Thorlabs). The images of the 5L color pixels in Figure 4 (b,c) and patterns in Figure 5 were obtained using a 4X objective lens (NA=0.1, Olympus Plan Achromat Objective) coupled with microscope (BX53 Olympus) coupled to by a CCD camera. The simple bubbling system consists of an air pump (LABOPORT N86), flowmeter (Brooks Instruments Direct FR Series), solvent bottle and hose. The air is pumped through the flowmeter through a solvent bottle into a flow-in and flow-out quartz sample cell (12.5 mm × 32.5 mm × 45mm).

SEM Imaging and Analysis: Scanning electron microscopy images of 11L arrays and 5L arrays and designed patterns were carried out using Zeiss Ultra scanning electron microscope, operating at 5 kV under SE2 mode. An Au-Pd nano-scale thin layer (~10 nm) was coated on the polymer structure as a conductive layer under argon atmosphere by coater (Cressington sputter coater 208HR). The Ag-Pd target (57 × 0.1 mm) for the coater was purchased from TED PELLA INC. The obtained top-down SEM images were analyzed in ImageJ software to measure linewidth. All Linewidth values mentioned herein are average values of ten manual measurements.

AFM imaging and Analysis: AFM imaging of the 2D spiral photonic arrays in air, Milli-Q water, and IPA was carried out using an MFP-3D AFM (Asylum Research). The AFM probe was a silicon tip (Budget Sensors, AIO-Cantilever-D, Sofia, Bulgaria) with an aluminum reflex coating, a resonance frequency of 300 kHz and a nominal cantilever stiffness of 40 Nm^{-1}. Imaging was performed in contact mode, height and deflection images were recorded. Data were recorded with 256 lines per scan direction at a scan angle of 90° and with a scan rate of 0.4Hz. All the topography images were flattened and presented with no further processing using Gwyddion (Czech Metrology Institute, Jihlava, Czech Republic, version 2.60). Line profile data was obtained following image postprocessing and plotted using Origin Pro 2020. Youngs modulus measurements were done in contact mode using the force spectroscopy technique in the Asylum software. Before doing force

curves on the sample, the probe is calibrated by performing 10 force distance curves on a glass slide and obtaining the spring constant and deflection InvOLS (Inverse Optical Lever Sensitivity). The modulus values are obtained by fitting the extension curve with the Hertz model. Force measurements are done in three different locations over the printed extended 11L spirals, and 3 force curves were collected at each point and the overall modulus value is reported by averaging 9 different forces curves.

Acknowledgement

This research received funding from the European Research Council (ERC) Starting Grant (No. 802929 – ChemLife), Science Foundation Ireland (SFI), and European Regional Development Fund (ERDF) under grant number 12/RC/2278_P2. JQ acknowledges funding from the Chinese Scholarship Council. ALB acknowledges SFI awards 16/IA/4550 and 17/RC-PhD/348. CD acknowledges support from the Irish Research Council through the Government of Ireland Postdoctoral Fellowship Scheme; Grant Number GOIPD/2020/484. LF also acknowledges funding from the European Horizon 2020 Research and Innovation Programme (No. 899349 – 5D NanoPrinting). We thank Mr. Christopher Smith for assistance with refractive index measurements of polymer films in Optical Analysis Lab (OAL). We acknowledge Mats Björklund and Magipics (https://magipics.com.au) for original graphics included in Figures 1 and 5. The TPP-DLW fabrication and the imaging for this project were carried out at the Additive Research Laboratory (AR-Lab) and the Advanced Microscopy Laboratory (AML), Trinity College Dublin, Ireland. The AR-Lab and AML are SFI supported centers, part of the CRANN Institute and affiliated to the AMBER Centre.

Conflict of Interest

The authors declare no conflict of interest.

References

[1] a) G. W. Ferguson, J. B. Murphy, J.-B. Ramanamanjato, A. Raselimanana, *The panther chameleon: color variation, natural history, conservation, and captive management*, Krieger

Publishing Company, **2004**; b) S. Kinoshita, S. Yoshioka, *ChemPhysChem* **2005**, 6, 1442; c) P. Wu, J. Wang, L. Jiang, *Materials Horizons* **2020**, 7, 338; d) Y. Yang, L. Wang, H. Yang, Q. Li, *Small science* **2021**, 1, 2100007.

[2] P. Vukusic, J. Sambles, C. Lawrence, R. Wootton, *Proceedings of the Royal Society of London. Series B: Biological Sciences* **1999**, 266, 1403.

[3] a) J. Teyssier, S. V. Saenko, D. Van Der Marel, M. C. Milinkovitch, *Nature communications* **2015**, 6, 1; b) J. Jones, J. Sanders, E. Segnit, *Nature* **1964**, 204, 990.

[4] a) W. Huang, S. Merzbach, C. Callenberg, D. Stavenga, M. Hullin, presented at ACM SIGGRAPH 2022 Conference Proceedings **2022**; b) D. G. Stavenga, J. Tinbergen, H. L. Leertouwer, B. D. Wilts, *Journal of Experimental Biology* **2011**, 214, 3960.

[5] a) P. Brady, M. Cummings, *The American Naturalist* **2010**, 175, 614; b) L. Wang, A. M. Urbas, Q. Li, *Advanced Materials* **2020**, 32, 1801335; c) V. Sharma, M. Crne, J. O. Park, M. Srinivasarao, *science* **2009**, 325, 449.

[6] W. Peng, S. Zhu, W. Wang, W. Zhang, J. Gu, X. Hu, D. Zhang, Z. Chen, *Advanced Functional Materials* **2012**, 22, 2072.

[7] D. E. Azofeifa, H. J. Arguedas, W. E. Vargas, *Optical materials* **2012**, 35, 175.

[8] T. M. Jordan, J. C. Partridge, N. W. Roberts, *Nature photonics* **2012**, 6, 759.

[9] a) W. Ma, Y. Kou, P. Zhao, S. Zhang, *ACS Applied Polymer Materials* **2020**, 2, 1605; b) J. Ren, Y. Wang, Y. Yao, Y. Wang, X. Fei, P. Qi, S. Lin, D. L. Kaplan, M. J. Buehler, S. Ling, *Chemical reviews* **2019**, 119, 12279; c) E. Wolde-Michael, A. D. Roberts, D. J. Heyes, A. G. Dumanli, J. J. Blaker, E. Takano, N. S. Scrutton, *Scientific reports* **2021**, 11, 1; d) H. S. Lim, J.-H. Lee, J. J. Walish, E. L. Thomas, *ACS nano* **2012**, 6, 8933; e) M. E. Calvo, H. Míguez, *Chemistry of Materials* **2010**, 22, 3909; f) I. Kriegel, F. Scotognella, *Optical Materials* **2022**, 123, 111859; g) P. M. Resende, M. Martín-González, *Materials Advances* **2022**, 3, 3199; h) M. Däntl, S. Guderley, K. Szendrei-Temesi, D. Chatzitheodoridou, P. Ganter, A. Jiménez-Solano, B. V. Lotsch, *Small* **2021**, 17, 2007864.

[10] a) Y. Wu, Y. Wang, S. Zhang, S. Wu, *ACS nano* **2021**, 15, 15720; b) E. S. Goerlitzer, R. N. Klupp Taylor, N. Vogel, *Advanced Materials* **2018**, 30, 1706654; c) G. H. Lee, T. M. Choi, B. Kim, S. H. Han, J. M. Lee, S.-H. Kim, *ACS nano* **2017**, 11, 11350; d) T. Liu, B. VanSaders, S. C. Glotzer, M. J. Solomon, *ACS applied materials & interfaces* **2020**, 12, 9842; e) H. K. Raut, H. Wang, Q. Ruan, H. Wang, J. G. Fernandez, J. K. Yang, *Nano Letters* **2021**, 21, 8602; f) C. Li, M. Zhao, X. Zhou, H. Li, Y. Wang, X. Hu, M. Li, L. Shi, Y. Song, *Advanced Optical Materials* **2018**, 6, 1800651; g) P. Liu, L. Bai, J. Yang, H. Gu, Q. Zhong, Z. Xie, Z. Gu, *Nanoscale Advances* **2019**, 1, 1672; h) S. L. Burg, A. J. Parnell, *Journal of Physics: Condensed Matter* **2018**, 30, 413001; i) B. M. Boyle, T. A. French, R. M. Pearson, B. G. McCarthy, G. M. Miyake, *ACS nano* **2017**, 11, 3052.

[11] a) Q. Ruan, W. Zhang, H. Wang, J. Y. E. Chan, H. Wang, H. Liu, D. Fan, Y. Li, C. W. Qiu, J. K. Yang, *Advanced Materials* **2022**, 34, 2108128; b) Y. Liu, H. Wang, J. Ho, R. C. Ng, R. J. Ng, V. H. Hall-Chen, E. H. Koay, Z. Dong, H. Liu, C.-W. Qiu, *Nature communications* **2019**, 10, 1; c) W. Zhang, H. Wang, H. Wang, J. Y. E. Chan, H. Liu, B. Zhang, Y.-F. Zhang, K. Agarwal, X. Yang, A. S. Ranganath, *Nature Communications* **2021**, 12, 1.

[12] a) D. Ge, E. Lee, L. Yang, Y. Cho, M. Li, D. S. Gianola, S. Yang, *Advanced Materials* **2015**, 27, 2489; b) H. S. Kang, S. W. Han, C. Park, S. W. Lee, H. Eoh, J. Baek, D.-G. Shin, T. H. Park, J. Huh, H. Lee, *Science advances* **2020**, 6, eabb5769.

[13] a) R. Zhang, Q. Wang, X. Zheng, *Journal of Materials Chemistry C* **2018**, 6, 3182; b) R. Hong, Y.

Shi, X.-Q. Wang, L. Peng, X. Wu, H. Cheng, S. Chen, *RSC advances* **2017**, 7, 33258.

[14] C. Zhou, Y. Qi, S. Zhang, W. Niu, S. Wu, W. Ma, B. Tang, *ACS Applied Materials & Interfaces* **2021**, 13, 26384.

[15] a) K. Li, J. Wang, W. Cai, H. He, M. Cen, J. Liu, D. Luo, Q. Mu, D. Gérard, Y. J. Liu, *Nano Letters* **2021**, 21, 7183; b) Z.-L. Zhang, X. Dong, Y.-N. Fan, L.-M. Yang, L. He, F. Song, X.-L. Wang, Y.-Z. Wang, *ACS Applied Materials & Interfaces* **2020**, 12, 46710.

[16] L. Brigo, A. Urciuolo, S. Giulitti, G. Della Giustina, M. Tromayer, R. Liska, N. Elvassore, G. Brusatin, *Acta biomaterialia* **2017**, 55, 373.

[17] a) C. Delaney, J. Qian, X. Zhang, R. Potyrailo, A. L. Bradley, L. Florea, *Journal of Materials Chemistry C* **2021**, 9, 11674; b) H. Wang, Q. Ruan, H. Wang, S. D. Rezaei, K. T. Lim, H. Liu, W. Zhang, J. Trisno, J. Y. E. Chan, J. K. Yang, *Nano Letters* **2021**, 21, 4721; c) H. Liu, H. Wang, H. Wang, J. Deng, Q. Ruan, W. Zhang, O. A. Abdelraouf, N. S. S. Ang, Z. Dong, J. K. Yang, *ACS nano* **2022**; d) J. Y. E. Chan, Q. Ruan, M. Jiang, H. Wang, H. Wang, W. Zhang, C.-W. Qiu, J. K. Yang, *Nature communications* **2021**, 12, 1; e) H. Wang, H. Wang, Q. Ruan, Y. S. Tan, C.-W. Qiu, J. K. Yang, *ACS nano* **2021**, 15, 10185; f) H. Wang, H. Wang, W. Zhang, J. K. Yang, *ACS nano* **2020**, 14, 10452; g) H. Gu, X. Liu, Z. Mu, Q. Wang, H. Ding, X. Du, Z. Gu, *ACS Applied Materials & Interfaces* **2021**, 13, 60648.

[18] a) Y. Dong, S. Wang, Y. Ke, L. Ding, X. Zeng, S. Magdassi, Y. Long, *Advanced Materials Technologies* **2020**, 5, 2000034; b) M. Champeau, D. A. Heinze, T. N. Viana, E. R. de Souza, A. C. Chinellato, S. Titotto, *Advanced Functional Materials* **2020**, 30, 1910606; c) S. B. Kumar, J. Jeevamalar, P. Ramu, G. Suresh, K. Senthilnathan, *Materials Today: Proceedings* **2021**, 45, 1433; d) M. Gao, Y. Meng, C. Shen, Q. Pei, *Advanced Materials* **2022**, 2109798.

[19] a) J. E. Harvey, R. N. Pfisterer, *Optical Engineering* **2019**, 58, 087105; b) M. Born, E. Wolf, *Principles of optics: electromagnetic theory of propagation, interference and diffraction of light*, Elsevier, **2013**; c) K. Knop, *JOSA* **1978**, 68, 1206.

[20] a) M. Carlotti, O. Tricinci, V. Mattoli, *Advanced Materials Technologies* **2022**, 2101590; b) L. R. Meza, A. J. Zelhofer, N. Clarke, A. J. Mateos, D. M. Kochmann, J. R. Greer, *Proceedings of the National Academy of Sciences* **2015**, 112, 11502; c) T. Limongi, L. Brigo, L. Tirinato, F. Pagliari, A. Gandin, P. Contessotto, A. Giugni, G. Brusatin, *Biomedical Materials* **2021**, 16, 035013.

[21] a) R. A. Potyrailo, R. K. Bonam, J. G. Hartley, T. A. Starkey, P. Vukusic, M. Vasudev, T. Bunning, R. R. Naik, Z. Tang, M. A. Palacios, *Nature communications* **2015**, 6, 1; b) R. A. Potyrailo, J. Brewer, B. Cheng, M. Carpenter, N. Houlihan, A. Kolmakov, *Faraday Discussions* **2020**, 223, 161; c) R. A. Potyrailo, J. Brewer, B. Scherer, V. Srivastava, M. Nayeri, C. Henderson, C. Collazo-Davila, M. Carpenter, N. Houlihan, V. V. Rossi, *ECS Transactions* **2019**, 91, 319.

[22] a) M. Malekovic, M. Urann, U. Steiner, B. D. Wilts, M. Kolle, *Advanced Optical Materials* **2020**, 8, 2000165; b) D. Kou, W. Ma, S. Zhang, B. Tang, *ACS Applied Polymer Materials* **2019**, 2, 2; c) M. Däntl, A. Jiménez-Solano, B. V. Lotsch, *Materials Advances* **2022**.

[23] Y. Liu, S. Wang, P. Biswas, P. Palit, W. Zhou, Y. Sun, *Scientific Reports* **2019**, 9, 1.

[24] a) L. Wang, J. Wang, Y. Huang, M. Liu, M. Kuang, Y. Li, L. Jiang, Y. Song, *Journal of Materials Chemistry* **2012**, 22, 21405; b) E. Tian, J. Wang, Y. Zheng, Y. Song, L. Jiang, D. Zhu, *Journal of Materials Chemistry* **2008**, 18, 1116.

[25] a) J. A. Kelly, A. M. Shukaliak, C. C. Cheung, K. E. Shopsowitz, W. Y. Hamad, M. J. MacLachlan, *Angewandte Chemie International Edition* **2013**, 52, 8912; b) M. Del Pozo, C. Delaney, C. W. Bastiaansen, D. Diamond, A. P. Schenning, L. Florea, *ACS nano* **2020**, 14, 9832.

[26] I. Z. Kozma, P. Krok, E. Riedle, *JOSA B* **2005**, 22, 1479.

[27] a) O. Levy, D. Stroud, *Physical Review B* **1997**, 56, 8035; b) S. Cunningham, C. Hrelescu, A. L. Bradley, *Optics Express* **2021**, 29, 22288.

[28] A. Tudor, C. Delaney, H. Zhang, A. J. Thompson, V. F. Curto, G.-Z. Yang, M. J. Higgins, D. Diamond, L. Florea, *Materials Today* **2018**, 21, 807.